



## Article

# Atmospheric HDO Abundance Measurements in the Tibetan Plateau Based on Laser Heterodyne Radiometer

Xingji Lu <sup>1,2</sup>, Yinbo Huang <sup>1,2</sup>, Pengfei Wu <sup>1,2</sup>, Jun Huang <sup>1,2</sup>, Tao Luo <sup>1,2</sup> , Qiang Liu <sup>1,2</sup> and Zhensong Cao <sup>1,2,\*</sup>

<sup>1</sup> Key Laboratory of Atmospheric Optics, Anhui Institute of Optics and Fine Mechanics, HFIPS, Chinese Academy of Sciences, Hefei 230031, China

<sup>2</sup> Advanced Laser Technology Laboratory of Anhui Province, Hefei 230037, China

\* Correspondence: zsciao@aiofm.ac.cn; Tel.: +86-18019963625

**Abstract:** The Tibet Plateau is known as the “third pole” of the world, and its environmental change profoundly impacts East Asia and even the global climate. HDO is the stable isotope of water vapor, which acts as an ideal tracer for studying the water cycle, and which is commonly used for atmospheric circulation and climatic studies. To monitor the water vapor isotopic abundance in the Tibetan Plateau, a portable laser heterodyne radiometer was operated in Golmud in August 2019. The radiometer utilizes a narrow-linewidth 3.66 μm distributed feedback interband cascade laser as the local oscillator, the heterodyne module is been optimized and the radiometer performs with high resolution and stability in obtaining spectral data. Furthermore, the absorption spectra of atmospheric HDO and H<sub>2</sub>O are obtained, and the retrieval method for water vapor isotopic abundance is discussed. The optimal estimation method is adopted to retrieve the density of HDO and H<sub>2</sub>O. The average column density of H<sub>2</sub>O was 1.22 g/cm<sup>2</sup>, and the HDO/H<sub>2</sub>O ratio in Golmud was  $178 \pm 15 \times 10^{-6}$  during the observation. For a better understanding of the retrieval, the retrieval errors are analyzed and compared. The results indicate that the smoothing error is significantly higher than the measurement error in this work. The backward trajectory analysis of atmospheric transport is used to investigate the relationship between water vapor density and atmospheric motion. The results indicate that the variation of H<sub>2</sub>O column density and HDO/H<sub>2</sub>O ratio have a relationship with atmospheric movements.

**Keywords:** laser heterodyne radiometer; isotopic abundance; atmospheric transportation; retrieval algorithm; backward trajectory analysis



**Citation:** Lu, X.; Huang, Y.; Wu, P.; Huang, J.; Luo, T.; Liu, Q.; Cao, Z. Atmospheric HDO Abundance Measurements in the Tibetan Plateau Based on Laser Heterodyne Radiometer. *Remote Sens.* **2024**, *16*, 459. <https://doi.org/10.3390/rs16030459>

Academic Editors: Tatiana Zhuravleva and Alexander Kokhanovsky

Received: 24 November 2023

Revised: 4 January 2024

Accepted: 14 January 2024

Published: 24 January 2024



**Copyright:** © 2024 by the authors. Licensee MDPI, Basel, Switzerland. This article is an open access article distributed under the terms and conditions of the Creative Commons Attribution (CC BY) license (<https://creativecommons.org/licenses/by/4.0/>).

## 1. Introduction

Monitoring the isotopic content of water vapor provides valuable information about the water cycle, including cloud feedback and radiation budgets, etc. [1,2]. Heavier water isotopologue HDO condenses more actively and evaporates less actively than the main isotopologue H<sub>2</sub><sup>16</sup>O, due to differences in the saturation vapor pressure of these two molecules. There are two stable isotopes of hydrogen, H with a relative abundance of 99.984%, and D with a relative abundance of 0.015%, and three stable isotopes of oxygen, <sup>16</sup>O, <sup>17</sup>O, and <sup>18</sup>O, with relative abundances of 99.759%, 0.037%, and 0.204%, respectively [3]. Since the numerical values of isotope abundance ratios in nature are very small, it is more convenient to describe the isotopic composition of a given water sample as the deviation of the abundance ratio from a standard value, expressed in per mil (‰). We have thus defined the delta notation defined as:

$$\delta D = 1000 \times \left[ \frac{\text{HDO}/\text{H}_2\text{O}}{\text{HDO}/\text{H}_2\text{O}_{\text{VSMOW}}} - 1 \right] \quad (1)$$

Here,  $\text{HDO}/\text{H}_2\text{O}$  is the ratio of HDO and  $\text{H}_2\text{O}$  abundance for a given water sample, and  $\text{HDO}/\text{H}_2\text{O}_{\text{VSMOW}}$  ( $=311.53 \times 10^{-6}$ ) is the  $\text{HDO}/\text{H}_2\text{O}$  of Vienna standard mean ocean water (VSMOW) [4].

The stable isotopes of HDO in the atmosphere are affected by various factors, such as latitude, altitude and distance from the coast, etc. [1,2]. For example, the international standards used for the determination of  $^{18}\text{O}$  and D isotope abundance ratios of VSMOW and Standard Light Antarctic Precipitation (SLAP) are  $155.76 \times 10^{-6}$  and  $89.1 \times 10^{-6}$ , respectively. However, the  $\delta\text{D}$  of SLAP is  $-428\text{‰}$  when referring to VSMOW [5]. The difference results in the depletion of HDO and indicates global and regional climate change [6,7]. Therefore, studying the isotopic composition of water vapor in the atmosphere is very helpful in identifying the sources and sinks of water cycling and climate change. Moreover, the variation in abundance is also related to ocean pollution, which helps in identifying the sources of pollution.

Due to its importance, in situ, ground-based and satellite remote sensing methods based on absorption spectroscopy methods have been developed for the measurement of water vapor isotopes. The in situ methods include Cavity Ring-Down Spectroscopy (CRDS), which is a kind of high sensitivity (precision is 5.65 ppm for  $\text{H}_2\text{O}$ ) technology for greenhouse gases detection [8,9]; this technology for HDO detection has recently been discussed by Michel et al. [10] and Chang et al. [11]. Michel used a quantum cascade laser to measure  $\text{H}_2^{16}\text{O}$  and  $\text{H}_2^{18}\text{O}$  spectra in  $7.2 \mu\text{m}$ , and the detection limit for  $\delta^{18}\text{O}$  was  $0.42\text{‰}$ . Chang used a  $2.65 \mu\text{m}$  tunable diode laser to measure  $\text{H}_2^{16}\text{O}$ ,  $\text{H}_2^{18}\text{O}$  and HDO spectra in different samples. The traditional instrument of ground-based methods is the Fourier Transform Infrared Radiometer (FTIR), such as the Total Carbon Column Observing Network (TCCON) and the Network for the Detection of Atmospheric Composition Change (NDACC). The data are usually used for the calibration of satellite observations [7,12]. The SCIAMACHY instrument on board the satellite ENVISAT was the first instrument to provide global retrievals of water isotopes with high sensitivity near the ground. However, due to degradation, the data record of SCIAMACHY HDO only covers the years 2003 through 2005, and unfortunately, the connection to the entire ENVISAT was lost in April 2012. Other studies on the global HDO distribution research based on GOSAT, AIRS and TROPOMI satellites were investigated, respectively, by Christian Frankenberg, Robert Herman and Andreas Schneider et al., and the results of these studies were compared and analyzed with data from TCCON [13–19]. Furthermore, the researchers have also paid much attention to the observation of Martian HDO abundance in recent years, because it provides unique insights into the evolution and climatology of its atmosphere [20,21]. The above studies show that the multiple methods of observation can provide more reliable results for determining the abundance of water vapor isotopes.

The analysis of monthly mean precipitation in Northwest China (NW) ( $35\text{--}50^\circ\text{N}$ ,  $74\text{--}105^\circ\text{E}$ ) indicates that the arid and semiarid regions of NW experienced a significant wetting trend in summer during 1961–2010. Undoubtedly, this trend had substantial effects on the ecological environment and social development, as well as the lives of people. In addition to the increased evaporation, the change in atmospheric circulation is another important factor [22]. The TP is known as ‘the third polar’ in geography, and its atmospheric exchange will influence East Asia and even the world’s climate. For this purpose, we are attempting to develop a new method for the water vapor isotopic abundance measurement and provide the fundamental data for the climatic research of NW and the TP. Therefore, it is significant to develop a portable device and carry out water vapor isotopic abundance measurements in order to enhance our understanding of climate change and atmospheric circulation.

In recent years, the laser heterodyne radiometer (LHR) has been greatly improved with high-quality performance in monitoring atmospheric trace gases at a small size and low cost, attracting lots of attention from related researchers. LHRs have been successfully used to measure atmospheric  $\text{O}_3$ ,  $\text{CO}_2$  and  $\text{CH}_4$ , etc., from the ground using either a quantum cascade laser (QCL) or distributed feedback (DFB) laser as a local oscillator (LO) [23–26].

Several laser heterodyne radiometers in the 3–5  $\mu\text{m}$  band were realized in our laboratory, and solar spectra through the entire atmosphere were obtained [27–29]. Accounting for the aforementioned reasons and fundamentals, we have developed an LHR operating at 3.66  $\mu\text{m}$  for monitoring atmospheric water vapor and its isotopic abundance.

In order to improve the data quality of the  $\text{H}_2\text{O}$  and its isotopic absorption spectrum, the combined ratio of laser to solar beam is optimized from 50%: 50% to 10%: 90%. The scanning time, the integral time and the filter band are optimized in this work for obtaining a high resolution and high signal-to-noise ratio. The spectral resolution is  $0.0098\text{ cm}^{-1}$ , theoretically. Additionally, the inversion method of water vapor isotope abundance was studied to realize the simultaneous inversion of  $\text{H}_2\text{O}$  and HDO column densities. The experimental campaign operated in Golmud ( $94.9^\circ\text{ E}$ ,  $36.4^\circ\text{ N}$ , Qinghai Province; the altitude is 2810 m) in August 2019. The synthetic spectra of HDO and  $\text{H}_2\text{O}$  were obtained simultaneously, and the HDO abundance was retrieved and analyzed.

## 2. Materials and Methods

### 2.1. Instrument Design and Operation

The simulation of the total atmospheric HDO and  $\text{H}_2\text{O}$  absorption spectrum by the Line-By-Line Radiative Transfer Model (LBLRM) at 3.66  $\mu\text{m}$  based on the standard atmospheric model (1976) is shown in Figure 1. The absorption intensity of HDO ( $\nu = 2730.9274\text{ cm}^{-1}$ ,  $S = 2.777 \times 10^{-24}\text{ cm}^{-1}/(\text{molec}\cdot\text{cm}^{-2})$ ) and  $\text{H}_2\text{O}$  ( $\nu = 2732.4932\text{ cm}^{-1}$ ,  $S = 1.206 \times 10^{-24}\text{ cm}^{-1}/(\text{molec}\cdot\text{cm}^{-2})$ ) is an optimal wavelength region in the mid-infrared. The absorption spectra of HDO and  $\text{H}_2\text{O}$  are within  $3\text{ cm}^{-1}$ , and the wavelength range can be covered in a single scanning by a diode laser. There is almost no interference absorption of other molecules in addition to  $\text{CH}_4$ . The laser heterodyne radiometer is an ideal instrument for this purpose, and the method can obtain an accurate of the HDO/ $\text{H}_2\text{O}$  ratio measurements.

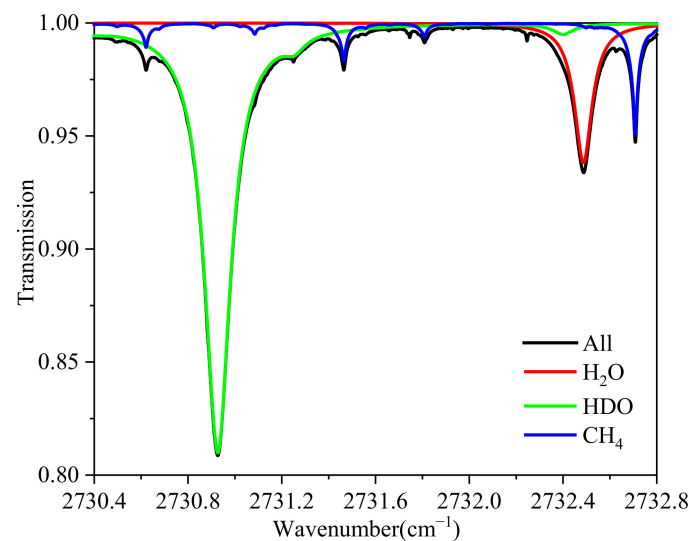


**Figure 1.** Simulated absorption spectra of HDO and  $\text{H}_2\text{O}$  at 3.66  $\mu\text{m}$ .

Laser heterodyne spectroscopy technology adopts a narrow linewidth laser to mix with the input signal light. The theoretical value of the total photocurrent generated by the detector is:

$$i = i_{DC} + i_{IF} = \frac{1}{2}\eta(A_{LO}^2 + A_S^2) + \eta A_{LO}A_S \cos(v_{LO} - v_S)t \quad (2)$$

where  $A_{LO}$  and  $A_S$  are the amplitude of  $LO$  and signal light,  $v_{LO}$  and  $v_S$  are the frequency of  $LO$  and signal light,  $\eta$  is the efficiency of the detector. The second item is the heterodyne signal and its power is:

$$\langle i_{IF}^2 \rangle = \left\langle \frac{1}{2}\eta^2 A_{LO}^2 A_S^2 \cos^2(v_{LO} - v_S)t \right\rangle = \frac{1}{2}\eta^2 P_{LO}P_S \quad (3)$$

where  $P_{LO}$  and  $P_S$  are the power of  $LO$  and signal light. The power of the heterodyne signal is proportional to the  $LO$  power and the signal light power. When the signal light power is weak, the light intensity information it carries can be amplified by the local oscillator light, the method can reduce the difficulties of spectral detection compared with direct detection. Then, the generated heterodyne signal is filtered, detected and demodulated to obtain the absorption spectrum signal of the atmospheric gases. The signal processing flow is shown in Figure 2.

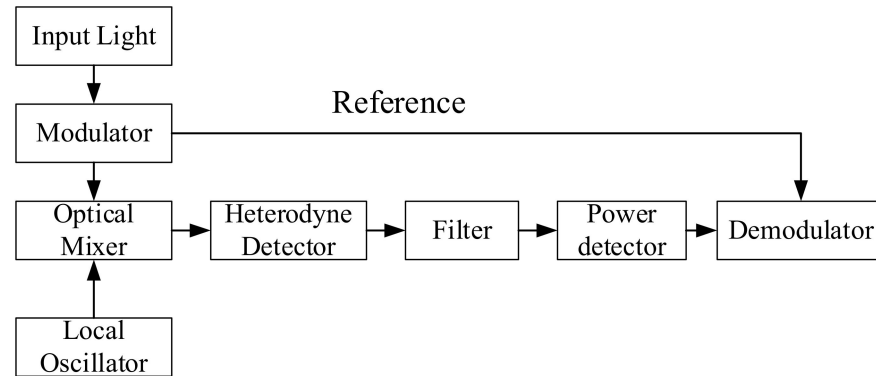


**Figure 2.** The diagram of laser heterodyne spectroscopy.

As shown in Figure 3a, the self-designed LHR consists of three modules: namely, the sun-tracking module, the heterodyning, and the signal-processing module [27–29]. The self-designed LHR utilizes a DFB interband cascade laser (ICL) as an  $LO$ , operating at  $3.66\ \mu\text{m}$  with a power output of several milliwatts (Nanosystems and Technologies, Meiningen, Germany). The DFB-ICL exhibits excellent performance in terms of narrow line width and continuous wavelength change in scanning mode, ensuring a high spectral resolution signal. The incoming sunlight is captured by a solar tracker and mixed with the  $LO$ . To promote the heterodyne signal, the combined ratio of the  $LO$  and sunlight is about 10%: 90%. The mixed light is focused by the off-axis parabolic (OAP) mirror and input into the detector. The focal length of the parabolic mirror is 2 inches, and the focus is located on the photosensitive surface of the detector. The PV-4TE-4 (VIGO Photonics, Warsaw, Poland) detector's sensitivity is up to  $1.0 \times 10^{11}\ \text{cm} \cdot \sqrt{\text{Hz}}/\text{W}$ , and its small active area ( $0.1\ \text{mm} \times 0.1\ \text{mm}$ ) and its temperature are controlled at 195 K, which can reduce the noise of the medium signal. The compact heterodyning module is shown in Figure 3b. Then the medium signal is processed by a radio frequency (RF) device and demodulated by a lock-in amplifier (LIA, OE1201, Sine Scientific Instruments, Guangzhou, China). A voltage noise as low as  $9\ \text{nV}/\sqrt{\text{Hz}}$  meets the demands of spectral measurements. In summary, the spectrum of the input signal can be obtained with high sensitivity by the LHR.

The HDO abundance based on the LHR is reported for the first time; the parameters of the LHR were comprehensively considered to obtain accurate absorption spectra of  $\text{H}_2\text{O}$  and HDO, such as scanning period, integral time and filter band. According to the signal-to-noise ratio (SNR) and instrumental line shape (ILS) of the LHR, the SNR is proportional to the integral time ( $\tau$ ) and filter band ( $B$ ), while the spectral resolution is inversely proportional to them [30].

$$\text{SNR} = \frac{2T_0\eta\sqrt{B/f_c}}{\exp(hv/kT_S) - 1} \quad (4)$$

$$\text{ILS} = f_{LO}(\omega) * H_B(\omega) * h_{f_c}(\omega) \quad (5)$$

In addition,  $f_c$  is the frequency of the low-pass filter, which is related to the integration time;  $f_{LO}(\omega)$  is the line shape function of the  $LO$ ;  $H_B(\omega)$  is the function of the bandpass filter in the frequency domain;  $h_{f_c}(\omega)$  is the function of the low-pass filter.

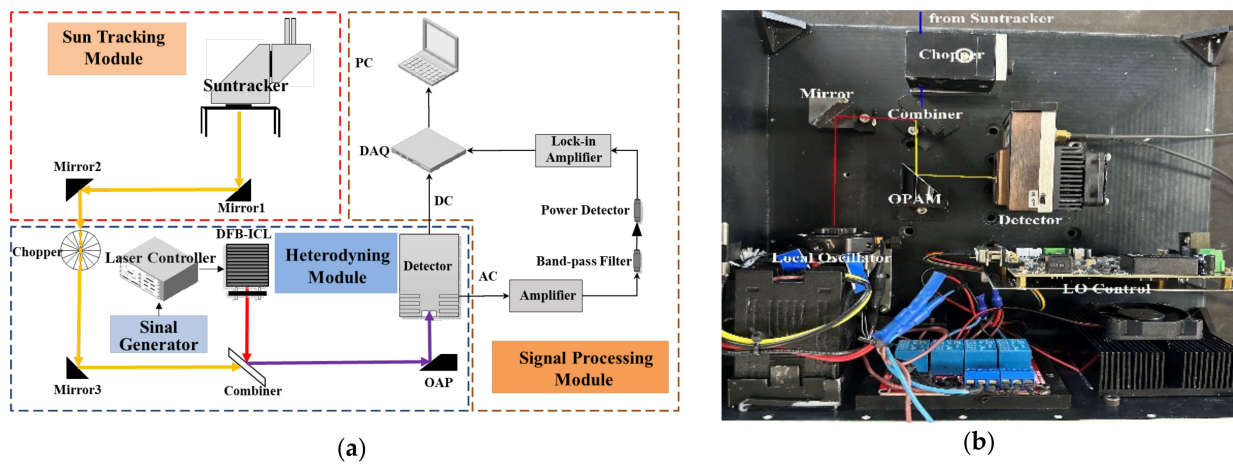


**Figure 3.** (a) The layout of laser heterodyne radiometer and (b) the compact heterodyning module.

The passband of the radio filter is 10~50 MHz (single bandwidth is 40 MHz, dual bandwidth is 80 MHz). The detailed parameters of the LHR are shown in Table 1.

**Table 1.** The detailed parameters of 3.66  $\mu\text{m}$  laser heterodyne radiometer.

Parameter	Value	Unit
Frequency coverage	2730.4~2732.8	$\text{cm}^{-1}$
Scanning period	15	s
Integral time	10	ms
Radio filter band	10~50	MHz
Average times	12	/

The simulated ILS of the LHR and the measured spectra with different integration times are shown in Figure 4. There are three suitable choices for the integral time of LIA, namely, 10 ms, 30 ms and 100 ms, and the corresponding spectral resolutions are  $0.0098 \text{ cm}^{-1}$ ,  $0.0194 \text{ cm}^{-1}$  and  $0.043 \text{ cm}^{-1}$ , respectively. The spectral bandwidth of  $\text{H}_2\text{O}$  and its isotope at 10 km is about  $0.018 \text{ cm}^{-1}$ . The integral time changed from 10 ms to 100 ms and the SNR increased, while the spectral resolution decreased. Additionally, the larger the integral time, the more obvious the delay effect. Therefore, the integral time was set to 10 ms in this study to achieve a more precise measurement of tropospheric water vapor and its isotopic spectrum.

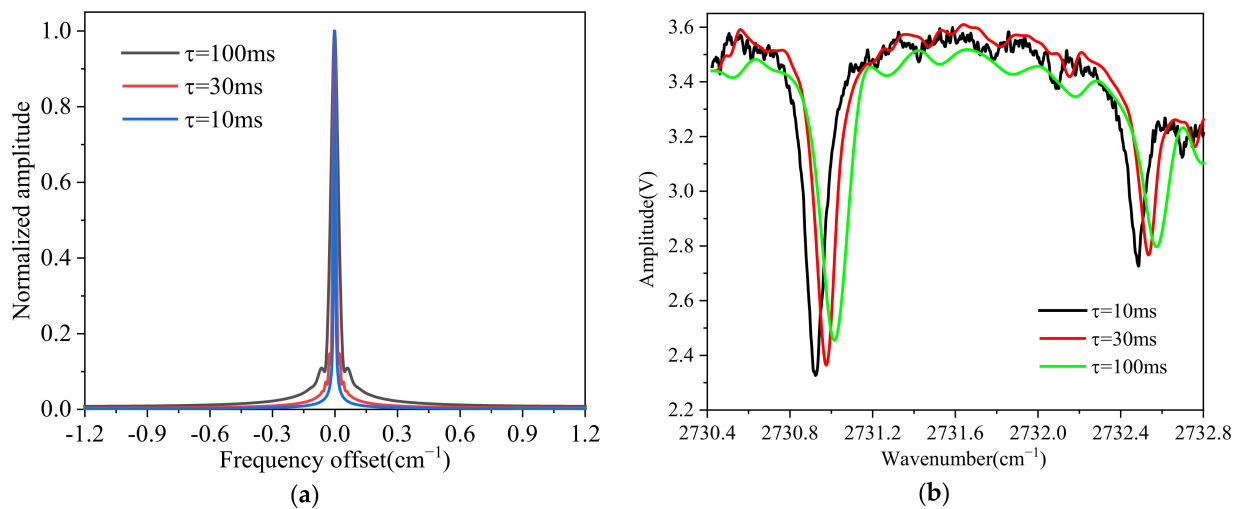


**Figure 4.** (a) The simulated ILS of LHR and (b) the measured spectra with different integration times.

Taking the change rates of water vapor density and solar angle into consideration, the acquisition period should be completed in several minutes. We chose a scanning period of 15 s with a 20% duty ratio, and the signal was averaged 12 times to improve the SNR. The total acquisition cycle costs 3 min in this case.

## 2.2. Experiment Site

Golmud is located at the outskirts of the Qaidam Basin and in the interior of the Tibetan Plateau (TP) (Figure 5). Because the annual average rainfall is only about 41.5 mm, while evaporation exceeds 3000 mm, Golmud is classified as having a continental plateau climate. Golmud is a typical city in NW and the TP; the research on atmospheric composition and exchange in this area helps to enhance our understanding of the climate of the TP and NW.



**Figure 5.** The location of the experiment site (red star in the enlarged map) in Golmud, Qinghai Province. The site is located near the western suburb of Golmud, the location can avoid the influence of the downtown as much as possible.

## 2.3. Retrieval Method

The measured heterodyne spectra were retrieved by the Optimal Estimation Method (OEM), the method was developed by C. Rodgers [31] and is widely used in atmospheric retrieval and obtains credible results with self-setting parameters, such as atmospheric layers, iterations and iteration type.

The progress of HDO/H<sub>2</sub>O inversion is shown in Figure 6. In this research, the LBLRTM (version 12.9), which is an accurate software for the research on atmospheric transmittance, radiative transfer and cooling rate [32], was used in the forward model for HDO and H<sub>2</sub>O density retrieval.

During the inversion in this research, HDO and H<sub>2</sub>O were treated as independent species without any side constraints (besides the similarity in the prior profile) imposed on the HDO–H<sub>2</sub>O functional relationship on the a priori covariance matrix. The density of HDO and H<sub>2</sub>O output individually. Another parameter, such as the continuum baseline fitted with a second-order polynomial, could reduce the influence of the LO scanning during the inversion.

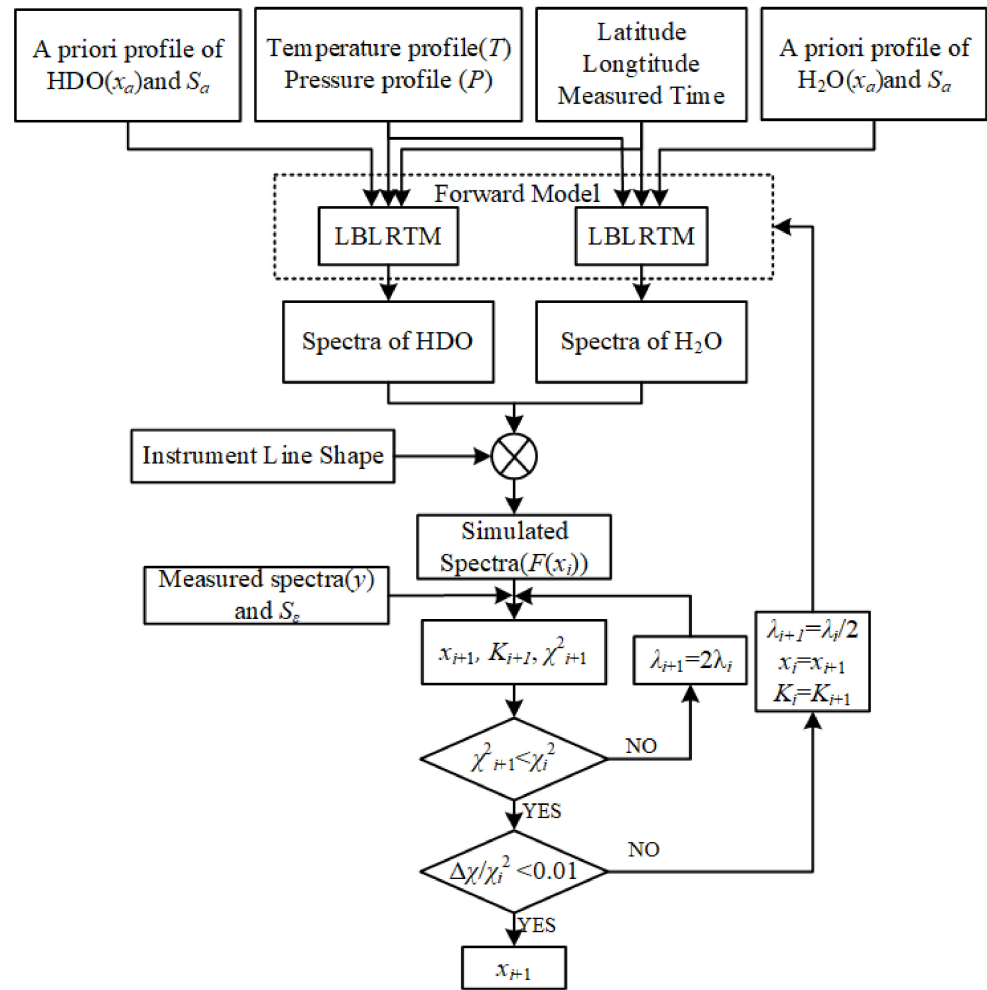


Figure 6. Flow chart of the retrieval method.

Additionally, the atmospheric model profiles of interfering species with weak absorption (mainly CH<sub>4</sub>) were adopted to reduce the difference. The temperature, a priori water vapor and methane profiles were obtained from the European Center for Medium-Range Weather Forecasts (ECMWF), as shown in Figure 7. The concentration of CH<sub>4</sub> was about 1.84 ppmv and almost unchanged below 15 km, while the concentration of water vapor changed greatly in three days and decreased exponentially with height; almost 90% of HDO and H<sub>2</sub>O was concentrated below 6 km altitude.

In the retrieval algorithm, the forward model  $F$  is defined by:

$$y = F(x) + \varepsilon \tag{6}$$

The vector  $y$  is the measured spectra with error  $\varepsilon$ ,  $x$  is the state vector of atmospheric profiles. The OEM is a Levenberg–Marquardt (LM) iterative algorithm based on the nonlinear-least-square method and minimizes the cost function to:

$$\chi^2 = (y - F)^T S_\varepsilon^{-1} (y - F) + (x_i - x_a)^T S_a^{-1} (x_i - x_a) \tag{7}$$

where  $S_\varepsilon$  and  $S_a$  are the measurement covariance matrix and a priori covariance matrix.  $x_a$  is the a priori vector. For the faster speed of iteration of the state vector, the Gauss–Newton iteration is used in the inversion:

$$x_{i+1} = x_i + \left[ K_i^T S_\varepsilon^{-1} K_i + (1 + \lambda_i) S_a^{-1} \right]^{-1} \times \left[ K_i^T S_\varepsilon^{-1} (y - F(x_i)) - S_a^{-1} (x_i - x_a) \right] \tag{8}$$

where  $K$  is the Jacobian matrix, and it is the important parameter that affects the retrieval results;  $\lambda$  is the Lagrange factor, and  $\lambda$  is chosen at each step to minimize the cost function; and the subscript represents the number of iterations [31]. The Jacobian matrix is calculated by:

$$K = \frac{\partial F(x)}{\partial x} \quad (9)$$

Each element is the partial derivative of a forward model element with respect to a state vector element, i.e.,  $K_{ij} = \partial F_i(x)/\partial x_j$ . The Jacobian value is the kernel parameter in the retrieval process, and it should be changed in each iteration, with an absolute value proportional to the intensity of absorption [31]. The Jacobian values of HDO and H<sub>2</sub>O are shown in Figure 8.

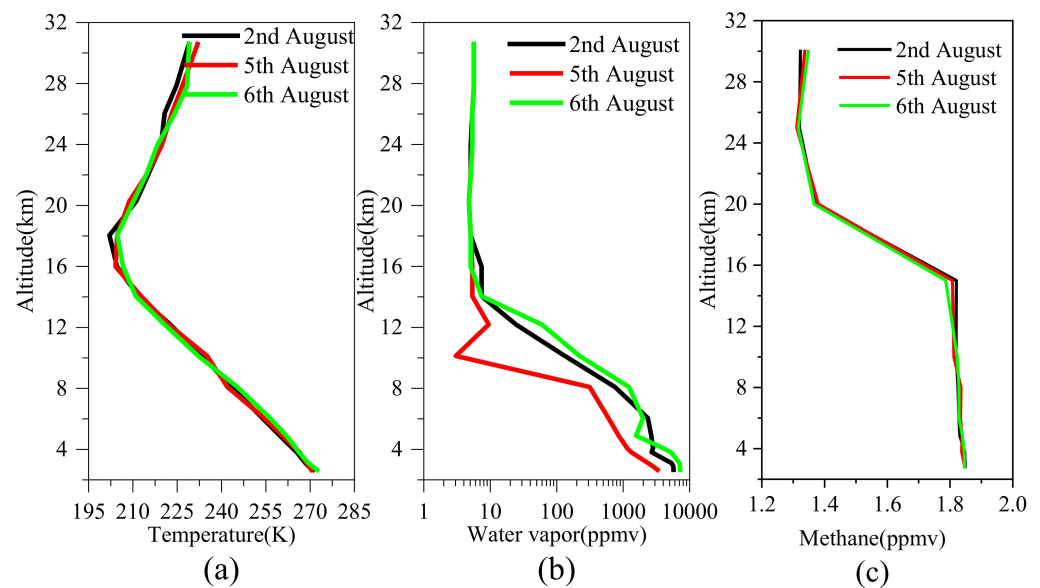


**Figure 7.** (a) Temperature profiles, (b) H<sub>2</sub>O profiles, and (c) CH<sub>4</sub> profiles on 2, 5 and 6 August from ECMWF.

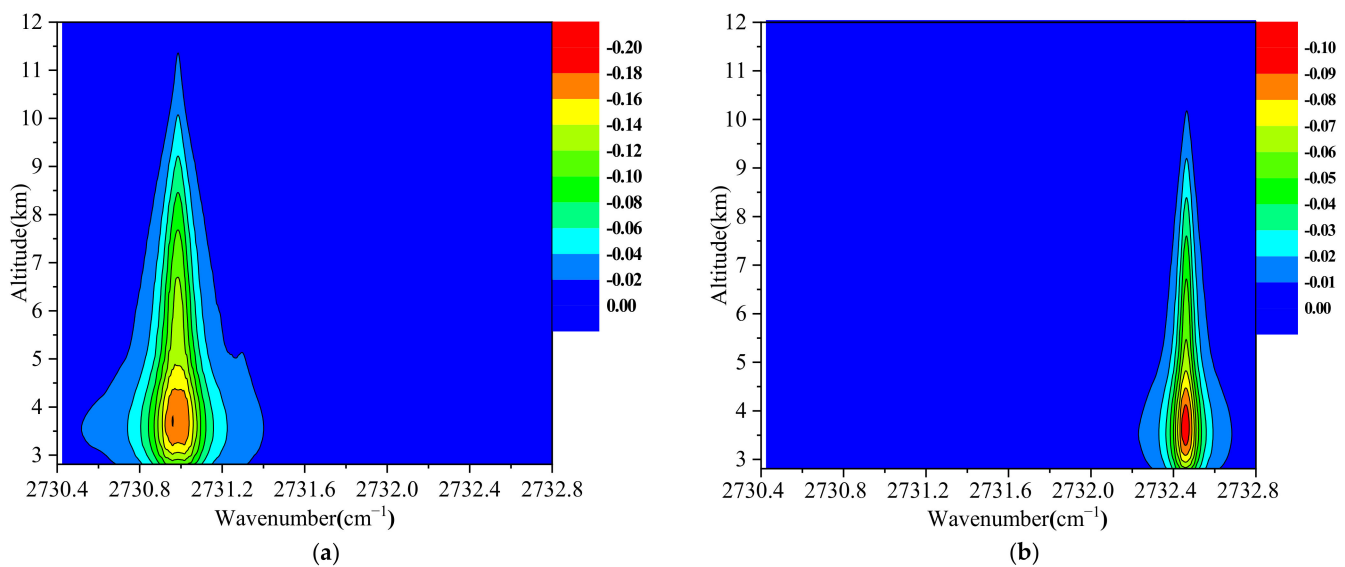


**Figure 8.** Jacobian values of (a) HDO and (b) H<sub>2</sub>O in 3.66  $\mu\text{m}$ .

Because of the big variation in water vapor density, the appropriate altitude grid is helpful for more precise retrieval results. The averaging kernel (AK) provides a simple characterization of the relationship between the retrieval and the actual state. The width of

the AK gives the vertical resolution of the instrument at the corresponding altitude, and the sum of the AK values is proportional to the information retrieved from the measurement rather than a priori [25]. The formula of the AK is described by:

$$A = \left( K^T S_\epsilon^{-1} K + S_a^{-1} \right) K^T S_\epsilon^{-1} K \quad (10)$$

The averaging kernels of H<sub>2</sub>O with 1 km spacing were calculated to optimize the altitude grid, and the results from the ground (2.81 km) to 30 km are shown in Figure 9.

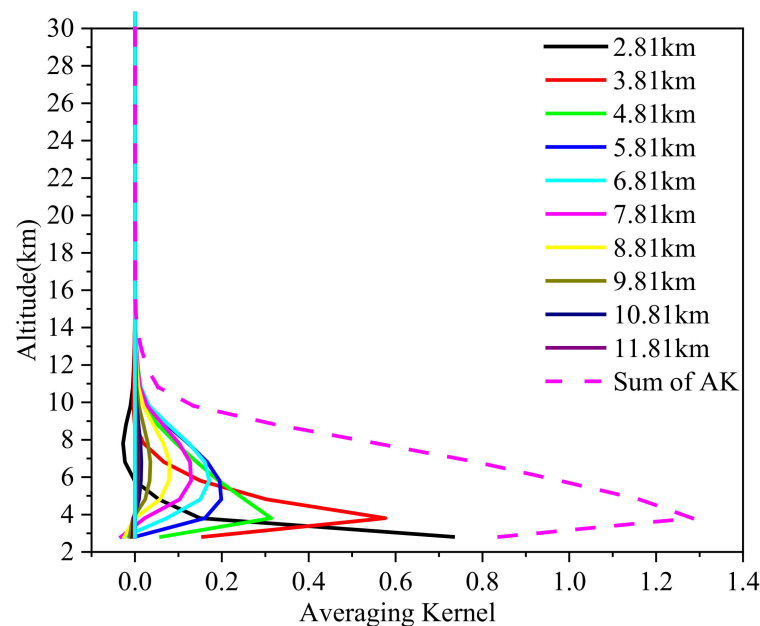


**Figure 9.** Averaging kernels with 1 km spacing.

Analysis of the averaging kernels shows that the half-width near the surface was 1~2 km, while the width above 4.81 km was much broader than the simulated 1 km resolution of the input altitude grid, indicating that much of the retrieved information was redundant.

Therefore, the retrieval layers were divided into 10 layers from the surface to 30 km. The height resolutions were 1 km (surface to 6 km), 2 km (6 km to 10 km) and 5 km (10 km to 30 km) respectively, accounting for the characteristics of atmospheric water vertical distribution. The averaging kernels were recalculated (Figure 10) after the refined altitude grid, the results indicate the altitude was almost associated with each AK peak, and the widths of AK below 8 km were more consistent with the altitude grid. The proper height spacing not only reduces the redundant information but also speeds up the calculation during the inversion.

Similar to the retrievals of other greenhouse gases in the mid-infrared, the sensitivity of inversion is much lower above 10 km; thus, the retrieval of profiles is not easily feasible, because the Jacobian and averaging kernel values of HDO and H<sub>2</sub>O are higher under 10 km than above 10 km. The densities of HDO and H<sub>2</sub>O can be retrieved from measured spectra, but it is extremely difficult for the retrieval process above 10 km. Hence, we focused on the retrieved total column amounts, which are more robust estimates in the mid-infrared.

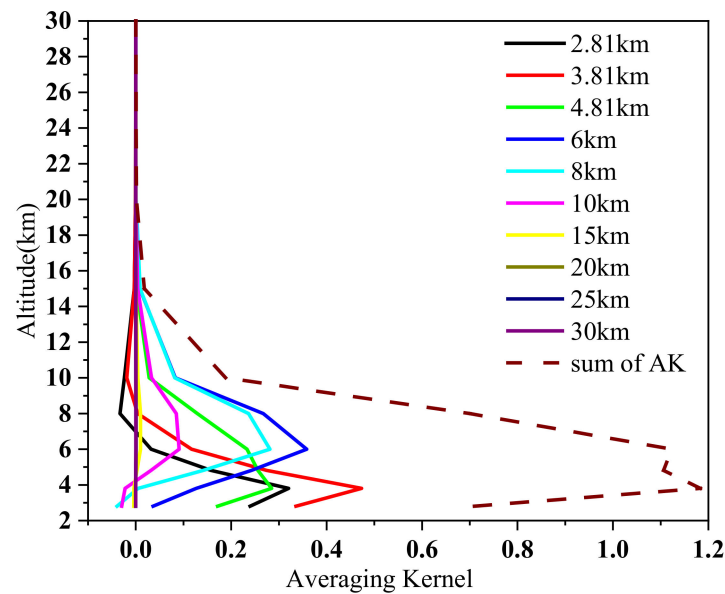


Figure 10. Averaging kernels with refined altitude grid.

### 3. Results

The SNR is the direct parameter that shows the performance of the LHR. The heterodyne signal and background signal (without sunlight input) were gathered before spectra measurement, and the SNR was 197.7 after being averaged 12 times (the SNR was about 57 without being averaged), as is shown in Figure 11. The capability ensured the high-quality data of spectra.

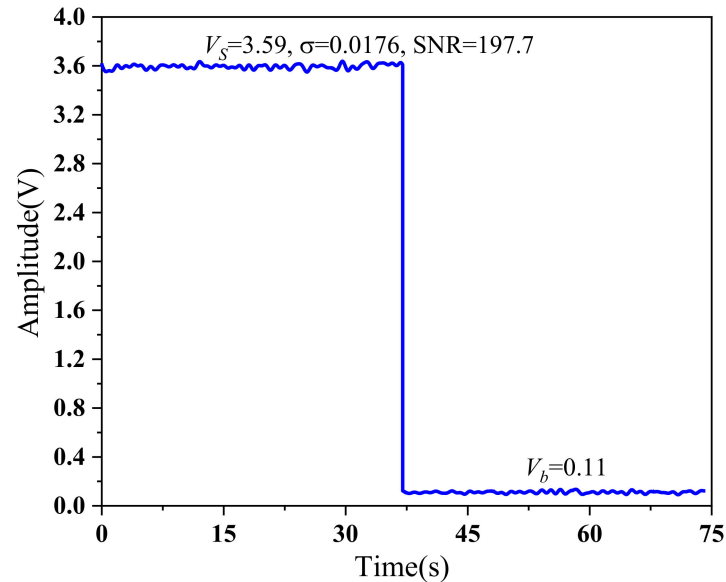
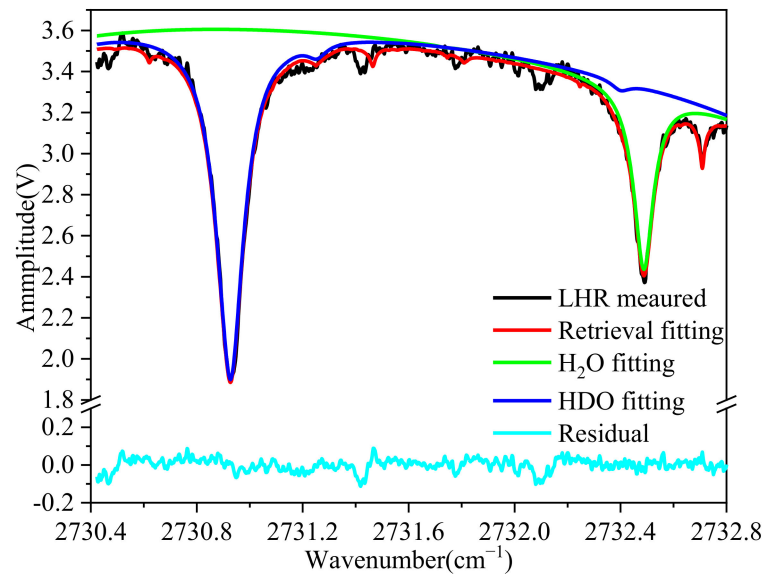


Figure 11. The signal-to-noise ratio (SNR) of 3.66  $\mu\text{m}$  LHR.

The OEM approach resulted in a more accurate fit to the measured spectrum. The absorption spectra of HDO and H<sub>2</sub>O were obtained respectively during the retrieval. One of the measured and retrieved fitting spectra is shown in Figure 12: the blue line is the fitted spectrum of HDO and the green line is the fitted spectrum of H<sub>2</sub>O, and the red line is the synthetic spectra of retrieval fitting. The residual was less than  $\pm 0.1$  V.



**Figure 12.** The measured (black line), the retrieval fitting (red line), H<sub>2</sub>O fitting (green line), HDO fitting (blue line) and the residual (light-blue line) spectrum.

The retrieved profiles and their variations of H<sub>2</sub>O and HDO, as well as the a priori profile from 2 August, are shown in Figure 13. Although the retrieved profiles and their variances were not accurate enough, they still provided meaningful information about the measurements and the progress of the retrieval.

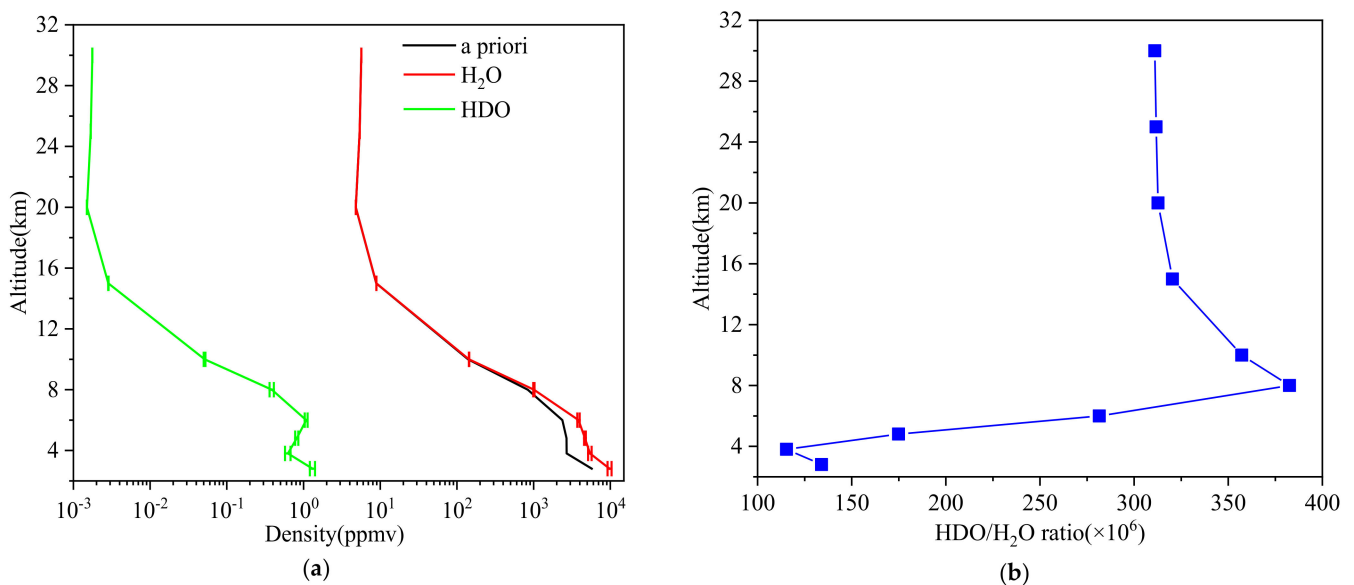


**Figure 13.** (a) Priori (black line), retrieved H<sub>2</sub>O (red line), and HDO (green line) profiles and (b) the HDO/H<sub>2</sub>O ratio profile on 2 August.

The retrieved profiles indicate that the measurements provide information on HDO and H<sub>2</sub>O distributions in the atmosphere below 10 km. However, in the upper atmosphere, the densities of HDO and H<sub>2</sub>O were significantly lower, and the LHR was not sensitive enough to detect them, as a result, the retrieved values in this range were almost identical to the prior profiles. The results suggest that the profiles of H<sub>2</sub>O and HDO could be retrieved in the lower troposphere based on LHR with higher sensitivity and a more comprehensive retrieval algorithm. The results suggest that it may be possible to retrieve the profiles of H<sub>2</sub>O and HDO in the lower troposphere using an LHR with increased sensitivity and a more comprehensive retrieval algorithm.

H<sub>2</sub>O column density and HDO/H<sub>2</sub>O ratio on 2, 5 and 6 August are shown in Figure 14. Measurements were suspended due to cloudy and rainy conditions on 3 and 4 August. During the experimental campaign, the column density of H<sub>2</sub>O was 1.07~1.4 g/cm<sup>2</sup> and the HDO/H<sub>2</sub>O ratio in Golmud was  $163 \times 10^{-6}$ ~ $193 \times 10^{-6}$ . More specifically, the daily average H<sub>2</sub>O column density for three consecutive days was 1.14 g/cm<sup>2</sup>, 1.32 g/cm<sup>2</sup> and 1.20 g/cm<sup>2</sup>, and the HDO/H<sub>2</sub>O ratio was  $185.05 \times 10^{-6}$ ,  $180.20 \times 10^{-6}$ , and  $183.27 \times 10^{-6}$  respectively. The measured HDO/H<sub>2</sub>O ratio was much lower than VSMOW, with a  $\delta D$  value of  $-476\%$ ~ $-380.5\%$ , and the average  $\delta D$  over three days was approximately  $-413\%$ . As a reference, the average  $\delta D$  retrieved based on GOSAT data in June, July and August from 2009~2011 around Golmud were approximately  $-350\%$  [16], with a relative difference of  $\sim 18\%$  to our results. Not only do the sensitivity of the LHR and the precision of parameters in the retrieval algorithm contribute to the differences, but the long-term and wide-range data averaging of satellite data could also be another significant factor. For a better understanding of the variations in atmospheric water vapor and its isotopes, the detailed analysis of water vapor density and the fluctuation of the HDO/H<sub>2</sub>O ratio in Golmud will be presented in the next subsection.

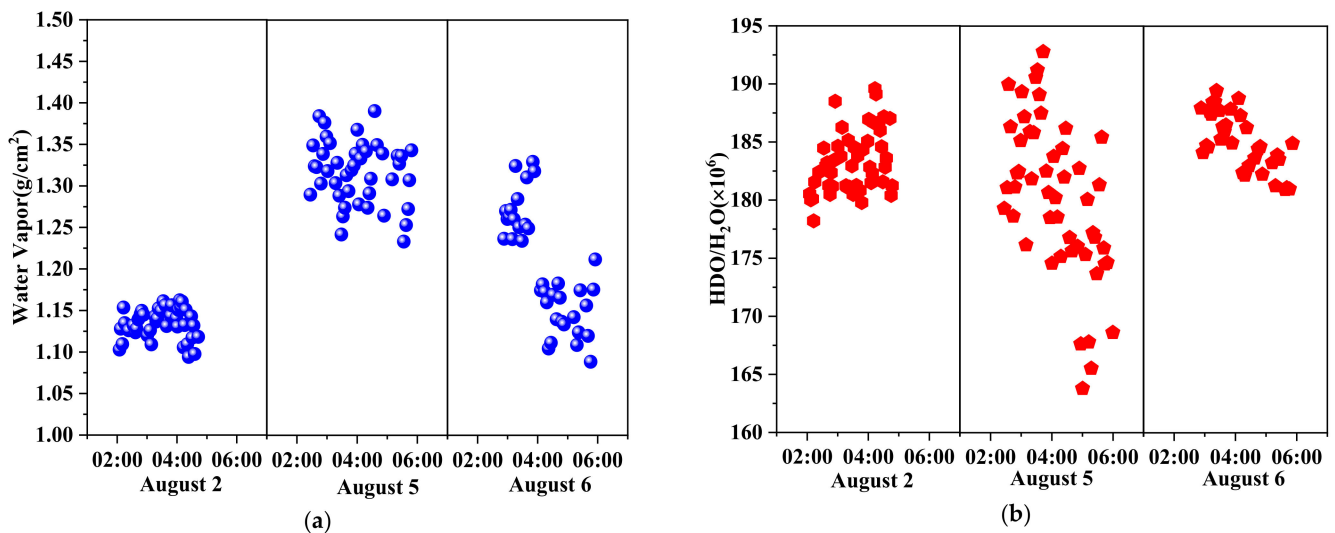


**Figure 14.** (a) H<sub>2</sub>O column density and (b) HDO/H<sub>2</sub>O ratio in Golmud measured by LHR.

## 4. Discussion

### 4.1. Error Analysis

The total error of the retrieved profile can be separated into three components. Due to error propagation, the error covariance matrix of the total error can be written as:

$$S_{tot} = S_s + S_m + S_f \quad (11)$$

$S_s$  is the smoothing error covariance matrix,  $S_m$  is the retrieval noise covariance matrix, and  $S_f$  is the forward model error covariance matrix. The forward model (LBLRTM) has high precision for atmospheric transmittance calculation, therefore the error of the forward model during the retrieval progress is smaller than other kinds of errors. Thus, the smoothing error and the retrieval noise error are concerns in the research. The error covariance matrix  $S_s$  can be calculated as:

$$S_s = \left( K^T S_\varepsilon^{-1} K + S_a^{-1} \right)^{-1} S_a^{-1} \left( K^T S_\varepsilon^{-1} K + S_a^{-1} \right)^{-1} \quad (12)$$

where  $S_a$  is the error covariance matrix of the a priori profile. Rodgers refers to  $S_s$  as the smoothing error, as this covariance matrix corresponds to portions of the profile space the measurements cannot see due to smoothing [31]. Those portions are the altitudes in the troposphere and small-scale variations obscured by the limited altitude resolution of

the profile retrieval. The smoothing error covariance matrix  $S_s$  is the weighted a priori covariance matrix  $S_a$  using  $(A - I)$  as weights. The error covariance matrix  $S_m$  can be calculated as:

$$S_m = \left( K^T S_\varepsilon^{-1} K + S_a^{-1} \right)^{-1} K^T S_\varepsilon^{-1} K \left( K^T S_\varepsilon^{-1} K + S_a^{-1} \right)^{-1} \quad (13)$$

where  $S_\varepsilon$  is the covariance matrix of the measurement error. The measurement error has to be assumed to be random, unbiased, and uncorrelated between measurement channels due to missing information. The measurement error includes noise of optical components, photon noise, and noise of the detector and amplifier. The measurement error is due to noise in the measurements propagating into the retrieval. The smoothing error and measurement error of  $H_2O$  and HDO were as follows.

As shown in the Figure 15, the smoothing error of the  $H_2O$  and HDO inversion results was greater than the measurement error, which indicates that the noise of the laser heterodyne radiometer was relatively low. Additionally, below 10 km altitude, the smoothing error and measurement error of  $H_2O$  and HDO were small. The possible reason is the high concentration of water vapor in the troposphere and the heterodyne radiometer can accurately measure the absorption spectra of  $H_2O$  and HDO while the water vapor concentration is very low above 10 km, but the sensitivity of the laser heterodyne spectrometer makes it difficult to obtain the absorption spectra accurately in this range, then leading to the stable smooth error and the change of the measurement error.

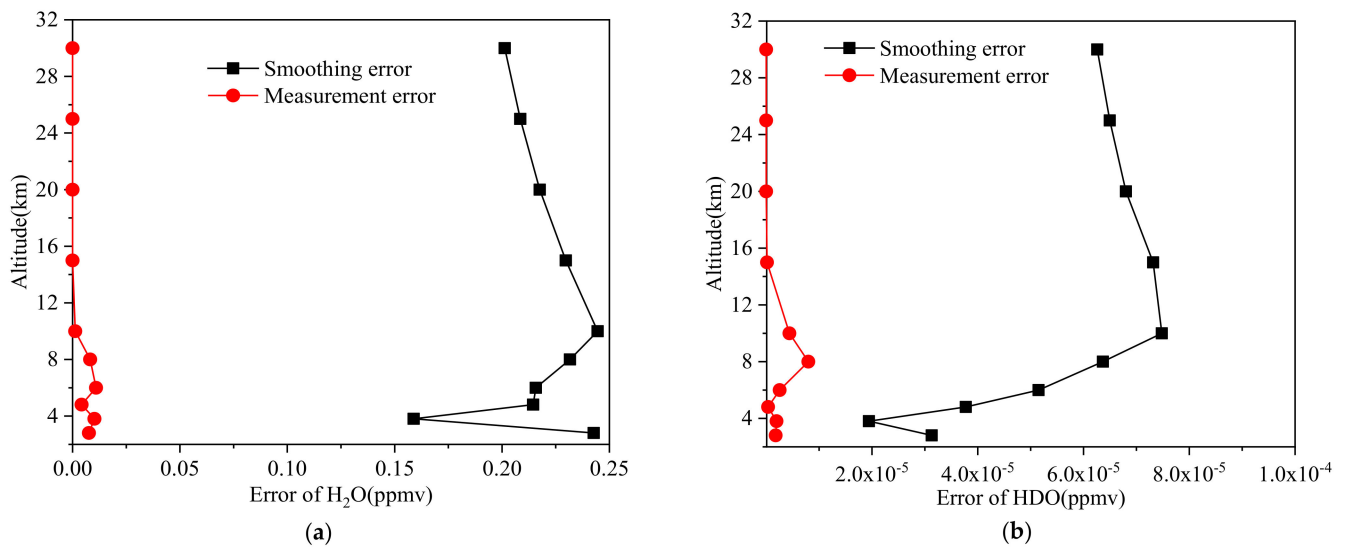


**Figure 15.** (a) Retrieval errors of  $H_2O$  and (b) retrieval errors of HDO.

#### 4.2. Analysis of $H_2O$ and HDO Variation

The Hybrid Single-Particle Lagrangian Integrated Trajectory model (HYSPPLIT) is a powerful tool for investigating the transport, dispersion and chemical transformation of atmospheric compositions. It was adopted here to explore the possible sources and transport pathways of atmospheric  $H_2O$  and HDO in Golmud, as well as the reasons for their variations during the experiment. Seventy-two-hour backward trajectories ending at 500 m, 2000 m and 3000 m above ground level (AGL) were performed at 00:00, 02:00, 04:00 and 06:00 on 2, 5 and 6 August. The results of backward trajectories are shown in Figures 16–18.

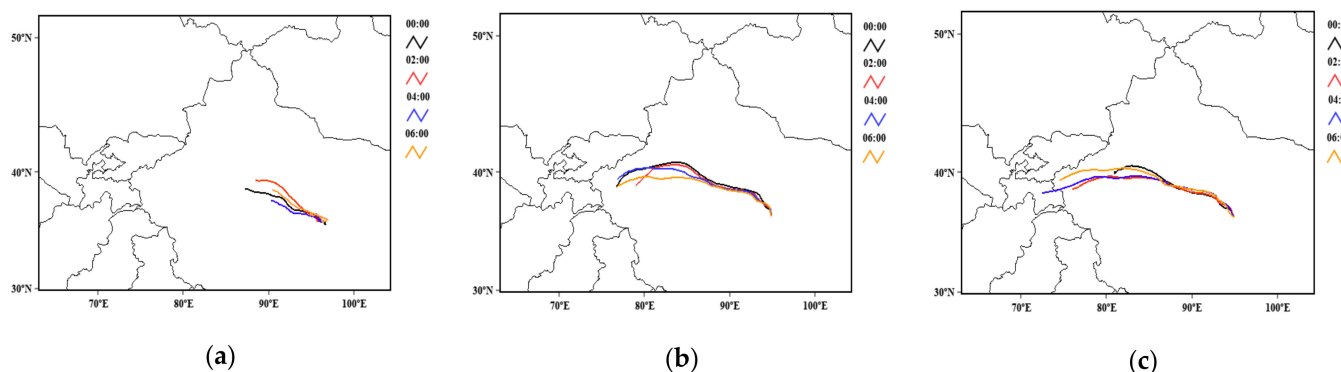


Figure 16. Backward trajectory on 2 August at (a) 500 m, (b) 2000 m and (c) 3000 m AGL.

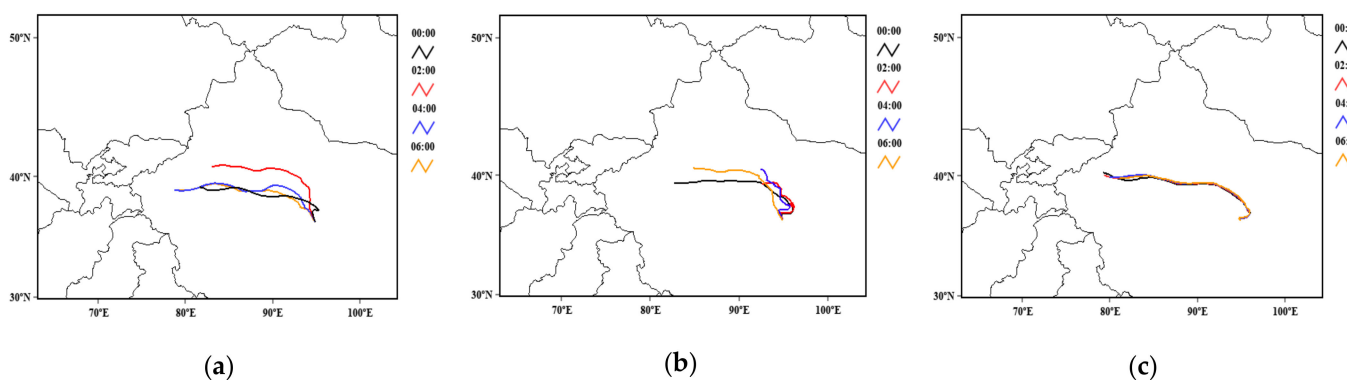


Figure 17. Backward trajectory on 5 August at (a) 500 m, (b) 2000 m and (c) 3000 m AGL.

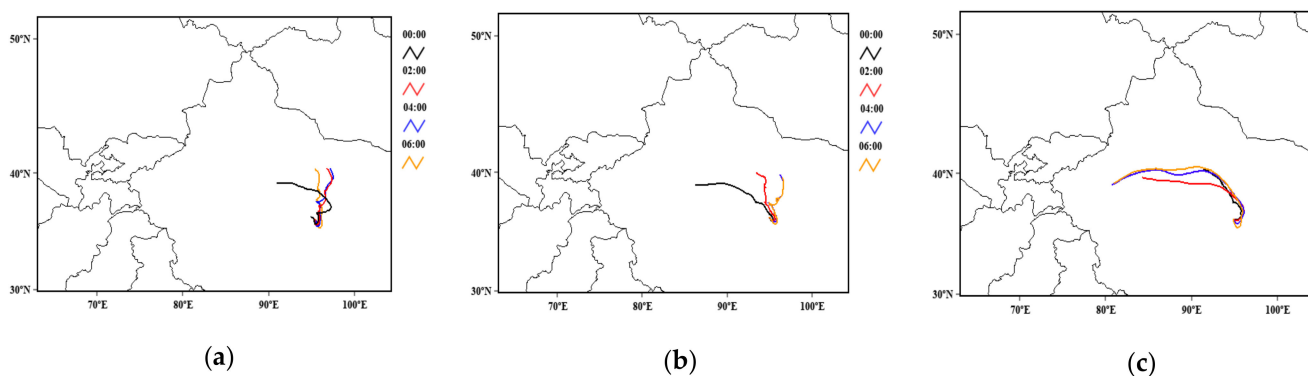


Figure 18. Backward trajectory on 6 August at (a) 500 m, (b) 2000 m and (c) 3000 m AGL.

According to the backward trajectory analysis, the starting point of the trajectories from 500 m to 3000 m AGL is in the NW. Specifically, water vapor and its isotopes in Golmud are mainly influenced by Xinjiang, Inner Mongolia, Gansu and Qinghai Province.

In particular, the original location and trajectory near the ground on 2 August were more stable than those on other days. Additionally, the variation in water vapor density and HDO/H<sub>2</sub>O ratio was the smallest over these three days. In contrast, the origin and the trajectories on 5 August were unstable during the observation, and the variation of water vapor density and HDO/H<sub>2</sub>O ratio was the largest among the three days. On 6 August, the original location and pathways from 02:00 to 04:00 were consistent at 500 m AGL. However, they changed around 04:00. The starting point and trajectory at 06:00 are different from those at 02:00 and 04:00. The time at which water vapor density changes was generally synchronized with changes in atmospheric motion. The water vapor densities on 2 and 6 August were lower than on 5 August, this may have been due to the light rain in Golmud on the evening of 3 August, which increased the ground humidity, and the evaporation

was larger on 5 August than the other two days. Through the analysis of the backward trajectory, it is speculated that the water vapor densities were related to the start points and the motivation of the atmosphere.

Therefore, there is a relationship between the water vapor density, the HDO/H<sub>2</sub>O ratio and atmospheric movement. The results indicate that the measurements of H<sub>2</sub>O density and HDO abundance could provide valuable information for research on atmospheric composition exchange and circulation.

## 5. Conclusions

The laser heterodyne radiometer is a powerful instrument used to obtain high-resolution solar spectra transmitted through the atmosphere. Despite its small size, it provides convenience for a wide range of atmospheric measurements. The self-built 3.66 μm LHR was successfully operated in Golmud in August 2019. The atmospheric H<sub>2</sub>O and HDO spectra were obtained using a new retrieval approach based on the optimal estimation method with LBLRTM as the forward model. Then, the column density of H<sub>2</sub>O and the ratio of HDO/H<sub>2</sub>O were investigated. The column density of H<sub>2</sub>O was 1.07~1.4 g/cm<sup>2</sup> and the HDO/H<sub>2</sub>O ratio in Golmud was  $163 \times 10^{-6}$ ~ $193 \times 10^{-6}$  during the experiment.

The analysis of the altitude grid optimized the better height spacing during the retrieval, the refined height layers reduced the redundant information. The retrieval errors were also analyzed in this work; the results indicate that the error in this work is mainly composed of smoothing error and measurement error, and the smoothing error is significantly higher than the measurement error. The retrieval error is related to the sensitivity of the laser heterodyne radiometer and the height distribution of water vapor and its isotope.

For a better understanding of the relationship between H<sub>2</sub>O (HDO) density and atmospheric motion, the research adopted backward trajectory analysis. Although the observations were not sufficient, the results indicate that the original location of airflow and the pathways influence the density of H<sub>2</sub>O and its isotopic abundance.

Therefore, the LHR can realize the measurements of column water vapor and isotopic ratio, and has the potential to retrieve H<sub>2</sub>O and HDO profiles in the lower troposphere. If long-term observation is carried out on the concerned sites, the variation regularity, sources and sinks of water vapor isotopes, and their relationship with atmospheric circulation can be further investigated. Recently, we have been working on improving the performance of the device. If possible, we plan to conduct long-term measurements in the TP or NW to gather more information on the abundance of HDO and environmental changes in this area. The study can help to gather data on atmospheric water vapor isotopes and improve the understanding of atmospheric circulation.

**Author Contributions:** Conceptualization, Y.H.; methodology, Z.C.; software, X.L.; formal analysis, X.L.; investigation, Z.C.; data curation, J.H.; writing—original draft preparation, X.L.; writing—review and editing, T.L., Q.L. and Z.C.; visualization, X.L.; supervision, Z.C.; project administration, P.W.; funding acquisition, P.W., T.L. and Z.C. All authors have read and agreed to the published version of the manuscript.

**Funding:** This research was funded by the Youth Innovation Promotion Association of the Chinese Academy of Sciences, grant numbers 2015264 and 2022450, and the Strategic Priority Research Program of the Chinese Academy of Sciences, grant number XDA17010104.

**Data Availability Statement:** Data are contained within the article.

**Acknowledgments:** The authors would like to thank the science teams of LBLRTM for the precise forward model. We also appreciate the teams at HITRAN for providing the high-quality and accessible data used in this study. Additionally, thanks to the teams at ECMWF provided the a priori profiles for the retrieval and teams at NOAA for providing the backward trajectory analysis in this work.

**Conflicts of Interest:** The authors declare no conflict of interest.

## References

1. Rosario, I. Development of a Near-Infrared Optical Feedback Cavity Enhanced Absorption Spectrometer (OF-CEAS) for Atmospheric Water Vapor Isotope Ratio ( $^{18}\text{O}/^{16}\text{O}$ ,  $^{17}\text{O}/^{16}\text{O}$ , and  $2\text{H}/1\text{H}$ ) Measurements. Ph.D. Thesis, University of Groningen, Groningen, The Netherlands, 2009; pp. 10–24.
2. Janek, L. Development of an OF-CEAS Laser Spectrometer for Water Vapor Isotope Measurements at Low Water Concentration. Ph.D. Thesis, University of Groningen, Groningen, The Netherlands, 2014; pp. 1–5.
3. Clark, I.D.; Fritz, P. *Environmental Isotopes in Hydrogeology*; Taylor & Francis Group: London, UK, 1997; pp. 1–8.
4. Hut, G. Consultants' group meeting on stable isotope reference samples for geochemical and hydrological investigations. *J. Geophys. Res.* **1987**, *42*, 1–44.
5. Gonfiantini, R. Standards for stable isotope measurements in natural compounds. *Nature* **1978**, *271*, 534–536. [[CrossRef](#)]
6. Kerstel, E.R.; Trigt, R.; Reuss, J.; Meijer, H.J. Simultaneous Determination of the  $^2\text{H}/^1\text{H}$ ,  $^{17}\text{O}/^{16}\text{O}$ , and  $^{18}\text{O}/^{16}\text{O}$  Isotope Abundance Ratios in Water by Means of Laser Spectrometry. *Anal. Chem.* **1999**, *71*, 5297–5303. [[CrossRef](#)] [[PubMed](#)]
7. Roktyan, N.V.; Zakharov, V.I.; Gribanov, K.G.; Schneider, M.; Breon, F.M.; Jouzel, J.; Imasu, R.; Werner, M.; Butzin, M.; Petri, C.; et al. A posteriori calculation of  $\delta^{18}\text{O}$  and  $\delta\text{D}$  in atmospheric water vapour from ground-based near-infrared FTIR retrievals of  $\text{H}_2^{16}\text{O}$ ,  $\text{H}_2^{18}\text{O}$ , and  $\text{HD}^{16}\text{O}$ . *Atmos. Meas. Tech.* **2014**, *7*, 2567–2580. [[CrossRef](#)]
8. Kerstel, E.R.; Gagliardi, G.; Gianfrani, L.; Meijer, H.A.J.; Trigt, R.; Ramaker, R. Determination of the  $^2\text{H}/^1\text{H}$ ,  $^{17}\text{O}/^{16}\text{O}$ , and  $^{18}\text{O}/^{16}\text{O}$  isotope ratios in water by means of tunable diode laser spectroscopy at 1.39  $\mu\text{m}$ . *Spectrochim. Acta Part A Mol. Biomol. Spectrosc.* **2002**, *58*, 2389–2396. [[CrossRef](#)] [[PubMed](#)]
9. Li, J.; Deng, H.; Sun, J.; Yu, B.; Fischer, H. Simultaneous atmospheric  $\text{CO}$ ,  $\text{N}_2\text{O}$  and  $\text{H}_2\text{O}$  detection using a single quantum cascade laser sensor based on dual-spectroscopy techniques. *Sens. Actuators B Chem.* **2016**, *231*, 723–732. [[CrossRef](#)]
10. Michel, A.M.; Wang, W.E.; Wang, L.; Nikodem, M.; Tsai, T.; Baeck, M.L.; Smith, J.; Wysocki, G. A Quantum Cascade Laser Spectrometer for Measurement of Water Vapor Isotopes in the Urban Environment. In Proceedings of the Conference on Lasers and Electro-Optics, San Jose, CA, USA, 6–11 May 2012.
11. Chang, A.; Visser, A.; Oerter, E.; Bond, T. Detection of  $\text{O}18$  and  $\text{D}$  Isotopes in Water Vapor using a Fiber-Coupled Tunable Diode Laser Absorption Spectroscopy Multi-Pass Cell. In Proceedings of the Conference on Lasers and Electro-Optics, San Jose, CA, USA, 13–18 May 2018.
12. Toptygin, A.Y.; Gribanov, K.G.; Zakharov, V.I.; Kasai, A.; Murayama, Y.; Imasu, R.; Schmidt, G.A.; Hoffmann, G.; Jouzel, J. Method and results of retrieval of  $\text{HDO}/\text{H}_2\text{O}$  in atmosphere from IMG/ADEOS and FTIR data. *Proc. SPIE* **2006**, *6580*, 240–245.
13. Worden, J.; Noone, D.; Galewsky, J.; Bailey, A.; Bowman, K.; Brown, D.; Hurley, J.; Kulawik, S.; Lee, J.; Strong, M. Estimate of bias in Aura TES  $\text{HDO}/\text{H}_2\text{O}$  profiles from comparison of TES and in situ  $\text{HDO}/\text{H}_2\text{O}$  measurements at the Mauna Loa observatory. *Atmos. Chem. Phys.* **2011**, *11*, 4491–4503. [[CrossRef](#)]
14. Lacour, J.L.; Clarisse, L.; Worden, J.; Schneider, M.; Barthlott, S.; Hase, F.; Risi, C.; Clerbaux, C.; Hurtmans, D.; Coheur, P.E. Cross-validation of IASI/MetOp derived tropospheric  $\delta\text{D}$  with TES and ground-based FTIR observations. *Atmos. Chem. Phys.* **2015**, *8*, 1447–1466. [[CrossRef](#)]
15. Scheepmaker, R.A.; Frankenberg, C.; Galli, A.; Butz, A.; Schrijver, H.; Deutscher, N.M.; Wunch, D.; Warneke, T.; Fally, S.; Aben, I. Improved water vapour spectroscopy in the 4174–4300  $\text{cm}^{-1}$  region and its impact on SCIAMACHY  $\text{HDO}/\text{H}_2\text{O}$  measurements. *Atmos. Meas. Tech.* **2013**, *5*, 8539–8578.
16. Frankenberg, C.; Wunch, D.; Toon, G.; Risi, C.; Scheepmaker, R.; Lee, J.E.; Wennberg, P.; Worden, J. Water vapor isotopologue retrievals from high-resolution GOSAT shortwave infrared spectra. *Atmos. Meas. Tech.* **2013**, *6*, 263–274. [[CrossRef](#)]
17. Herman, R.L.; Worden, J.; Noone, D.; Henze, D.; Bowman, K.; Pereira, K.C.; Payne, V.H.; Kulawik, S.S.; Fu, D.J. Comparison of Optimal Estimation  $\text{HDO}/\text{H}_2\text{O}$  Retrievals from AIRS with ORACLES measurements. *Atmos. Meas. Tech.* **2020**, *13*, 1825–1834. [[CrossRef](#)]
18. Schneider, A.; Borsdorff, T.; Brugh, J.; Aemisegger, F.; Feist, D.; Kivi, R.; Hase, F.; Schneider, M.; Landgraf, J. First data set of  $\text{H}_2\text{O}/\text{HDO}$  columns from the Tropospheric Monitoring Instrument (TROPOMI). *Atmos. Meas. Tech.* **2020**, *13*, 85–100. [[CrossRef](#)]
19. Zadvornykh, I.V.; Gribanov, K.G.; Denisova, N.Y.; Zakharov, V.I.; Imasu, R. Method for Retrieval of the  $\text{HDO}/\text{H}_2\text{O}$  Ratio Vertical Profile in the Atmosphere from Satellite Spectra Simultaneously Measured in Thermal and Near-IR Ranges. *Atmos. Ocean. Opt.* **2021**, *34*, 81–86. [[CrossRef](#)]
20. Aoki, S.; Nakagawa, H.; Sagawa, H.; Giuranna, M.; Sindoni, G.; Aronica, A.; Kasaba, Y. Seasonal variation of the  $\text{HDO}/\text{H}_2\text{O}$  ratio in the atmosphere of Mars at the middle of northern spring and beginning of northern summer. *Icarus* **2015**, *260*, 7–22. [[CrossRef](#)]
21. Khayat, A.S.J.; Villanueva, G.L.; Smith, M.D.; Guzewich, S.D. IRTF/CSHELL mapping of atmospheric  $\text{HDO}$ ,  $\text{H}_2\text{O}$  and  $\text{D}/\text{H}$  on Mars during northern summer. *Icarus* **2019**, *330*, 204–216. [[CrossRef](#)]
22. Peng, D.; Zhou, T. Why was the arid and semiarid northwest China getting wetter in the recent decades? *J. Geophys. Res.* **2017**, *122*, 9060–9075. [[CrossRef](#)]
23. Taguchi, M.; Okano, S.; Fukunishi, H.; Sasano, Y. Comparison of ozone profiles from ground-based laser heterodyne spectrometer and ozonesonde measurements. *Geophys. Res. Lett.* **1990**, *17*, 2349–2352. [[CrossRef](#)]
24. Weidmann, D.; Reburn, W.J.; Smith, K.M. Retrieval of atmospheric ozone profiles from an infrared quantum cascade laser heterodyne radiometer: Results and analysis. *Appl. Opt.* **2007**, *46*, 7162–7171. [[CrossRef](#)]
25. Tsai, T.R.; Rose, R.A.; Weidmann, D.; Wysocki, G. Atmospheric vertical profiles of  $\text{O}_3$ ,  $\text{N}_2\text{O}$ ,  $\text{CH}_4$ ,  $\text{CCl}_2\text{F}_2$ , and  $\text{H}_2\text{O}$  retrieved from external-cavity quantum-cascade laser heterodyne radiometer measurements. *Appl. Opt.* **2012**, *51*, 8779–8792. [[CrossRef](#)]

26. Melroy, H.R.; Wilson, E.L.; Clarke, G.B.; Ott, L.E.; Mao, J.; Ramanathan, A.K.; McLinden, M.L. Autonomous field measurements of CO<sub>2</sub> in the atmospheric column with the miniaturized laser heterodyne radiometer (Mini-LHR). *Appl. Phys. B* **2015**, *120*, 609–615. [[CrossRef](#)] [[PubMed](#)]
27. Tan, T.; Cao, Z.; Wang, G.; Wang, L.; Liu, K.; Huang, Y.; Chen, W.; Gao, X. Study on the technology of the 4.4 μm mid-infrared laser heterodyne spectrum. *Spectrosc. Spect. Anal.* **2015**, *35*, 60–63.
28. Lu, X.; Cao, Z.; Huang, Y.; Gao, X.; Rao, R. Laser heterodyne spectrometer for solar spectrum measurement in the 3.53 μm region. *Opt. Precise Eng.* **2019**, *26*, 16–24.
29. Wang, J.; Wang, G.; Tan, T.; Zhu, G.; Sun, C.; Cao, Z.; Chen, W.; Gao, X. Mid-infrared laser heterodyne radiometer (LHR) based on a 3.53 μm room-temperature interband cascade laser. *Opt. Express* **2019**, *27*, 9610–9619. [[CrossRef](#)]
30. Lu, X.; Huang, Y.; Wu, P.; Liu, D.; Ma, H.; Wang, G.; Cao, Z. Distributed Feedback Interband Cascade Laser Based Laser Heterodyne Radiometer for Column Density of HDO and CH<sub>4</sub> Measurements at Dunhuang, Northwest of China. *Remote Sens.* **2022**, *14*, 1489–1502. [[CrossRef](#)]
31. Rodgers, C.D. *Inverse Methods for Atmospheric Sounding*, 2nd ed.; World Scientific: London, UK, 2004; Volumes 4–5, pp. 65–100.
32. Chen, X.; Wei, H. Transplantation of LBLRTM from Workstation to PC. *J. Atmos. Environ. Opt.* **2007**, *2*, 99–103.

**Disclaimer/Publisher’s Note:** The statements, opinions and data contained in all publications are solely those of the individual author(s) and contributor(s) and not of MDPI and/or the editor(s). MDPI and/or the editor(s) disclaim responsibility for any injury to people or property resulting from any ideas, methods, instructions or products referred to in the content.